



Current perpendicular-to-plane giant magnetoresistance using an $L1_2$ Ag_3Mg spacer and $\text{Co}_2\text{Fe}_{0.4}\text{Mn}_{0.6}\text{Si}$ Heusler alloy electrodes: Spacer thickness and annealing temperature dependence

Takahide Kubota,^{1,2,*} Yusuke Ina,¹ Zhenchao Wen,^{1,2} Hiroyuki Narisawa,¹ and Koki Takanashi^{1,2}

¹Institute for Materials Research, Tohoku University, Sendai 980-8577, Japan

²Center for Spintronics Research Network, Tohoku University, Sendai 980-8577, Japan

(Received 13 May 2017; revised manuscript received 10 August 2017; published 13 September 2017)

Spacer thickness t_N and annealing temperature T_{anneal} dependence of current perpendicular-to-plane giant magnetoresistance effects were investigated in junctions using $L1_2$ Ag_3Mg spacer and half-metallic $\text{Co}_2\text{Fe}_{0.4}\text{Mn}_{0.6}\text{Si}$ (CFMS) Heusler alloy electrodes. t_N was changed from 2–12 nm and T_{anneal} was changed from 450–650 °C to promote the chemical ordering of the CFMS electrodes. Concerning the t_N dependence, the magnetoresistance (MR) ratio and the change of the areal resistance (ΔRA) exhibited the maximum values at $t_N = 5$ nm. The reasons for the decrease of the MR ratio for $t_N < 5$ nm and for $t_N > 5$ nm were possibly due to an unstable antiparallel magnetization configuration and to the increased occurrence of spin scattering inside the Ag_3Mg spacer, respectively. The spin-diffusion length of the Ag_3Mg spacer was also estimated using the t_N dependence of ΔRA and it was found to be of the order of 10–30 nm. Concerning the T_{anneal} dependence, ΔRA and the MR ratio exhibited the maximum values at 550 °C, which was the optimum point in terms of the degrees of order in the CFMS layers and the Ag_3Mg layer, and the (001) orientation of the layered structure. The maximum ΔRA and the intrinsic MR ratio in which parasitic resistance contribution was eliminated were 25 $\text{m}\Omega \mu\text{m}^2$ and 63%, respectively, at room temperature.

DOI: 10.1103/PhysRevMaterials.1.044402

I. INTRODUCTION

The amount of data in the world has increased drastically in recent decades because of the widespread cloud computing and coming society based on Internet of Things (IoT). The hard disk drive (HDD) is an established storage device for storing a large volume of data with a relatively low cost and it is expected that the recording density will reach of the order of several terabits per square inch in the coming decades [1]. Enhancement of read head sensitivity is a task for the future HDD development, and half-metallic Heusler-alloy-based giant magnetoresistive (GMR) junctions with current perpendicular-to-plane (CPP) geometry are a solution [2], which may realize a relatively large MR effect with a junction resistance range of 10–100 $\text{m}\Omega \mu\text{m}^2$ in the resistance area product (RA) value [3,4]. CPP-GMR junctions using cobalt (Co)-based full-Heusler alloys have been extensively studied since the reports of relatively large MR ratios and changes of the areal resistance (ΔRA) in $\text{Co}_2\text{MnSi} | \text{Cr} | \text{Co}_2\text{MnSi}$ junctions at room temperature [5,6]. Among the several compositions of Co-Heusler alloys studied for CPP-GMR junctions [7–14], $\text{Co}_2\text{Fe}_{0.4}\text{Mn}_{0.6}\text{Si}$ (CFMS) has been selected in this work, which is an optimum composition for the high MR ratio [13] and a high exchange stiffness at the interface between CFMS and a spacer, e.g., Ag [15,16]. A choice of the spacer material is also a crucial matter for the Heusler-based CPP-GMR junctions. A typical example is that Ag-spacer junctions with Co_2MnSi electrodes exhibit a larger MR ratio and ΔRA than Cr-spacer junctions, which is caused by a good matching of the band-dispersion curves in the $\text{Co}_2\text{MnSi} | \text{Ag} | \text{Co}_2\text{MnSi}$ [17]. Several spacer materials have also been studied in light of the band matching to Co-Heusler alloy electrodes; e.g.,

nonmagnetic Heusler alloys Ru_2CuSn [18] and Cu_2TiAl [19], $B2$ -NiAl alloy [20,21], Cu-Zn alloy [22], semiconductive materials In-Zn-O [23], $\text{Cu}(\text{In}_{0.8}\text{Ga}_{0.2})\text{Se}_2$ [24–26], and so on. We have focused on an $L1_2$ -type Ag_3Mg alloy [27,28] for the spacer material and demonstrated a large MR ratio and ΔRA in experiments, as well as the theoretically proposed good band matching to the CFMS Heusler alloy [29–32]. However, some experimental conditions, such as the spacer thickness and the annealing temperature for all layers, were fixed in the previous $L1_2$ -type Ag_3Mg spacer junctions [29,31]. According to some earlier studies, CPP-GMR was sensitive to both spacer thickness [11,19] and annealing temperature [9,15,22]: A thinner spacer makes CPP-GMR larger because the spin scattering possibly occurs less with a shorter propagation length inside the spacer, and the annealing temperature affects the chemical ordering of CFMS layers, which changes the spin polarization. In this study, we therefore investigated the dependence on these parameters for the CFMS $| L1_2 \text{Ag}_3\text{Mg} |$ CFMS junctions.

II. EXPERIMENTAL PROCEDURES

Layered films were deposited onto a single-crystalline MgO(100) substrate using an ultrahigh-vacuum magnetron sputtering system with a base pressure below 1×10^{-7} Pa. The stacking structure was MgO sub. $| \text{Cr}$ (20 nm) $| \text{Ag}$ (40 nm) $| \text{CFMS}$ (20 nm) $| \text{Ag}_3\text{Mg}$ (t_N) $| \text{CFMS}$ (7 nm) $| \text{Ag}$ (2 nm) $| \text{Au}$ (5 nm), from bottom to top, where the numbers in parentheses are the layer thicknesses. The film compositions of the CFMS and Ag_3Mg layers were $\text{Co}_{47}\text{Fe}_{13}\text{Mn}_{15}\text{Si}_{25}$ (at.%) and $\text{Ag}_{78}\text{Mg}_{22}$ (at.%), respectively. The spacer thicknesses t_N were 2, 3, 5, 7, 10, and 12 nm. The deposition temperature was an ambient temperature for all the layers, and postannealing was performed at 650 °C after the depositions of the Cr layer to achieve a flat surface. Another annealing procedure was

*Author to whom correspondence should be addressed: tkubota@imr.tohoku.ac.jp

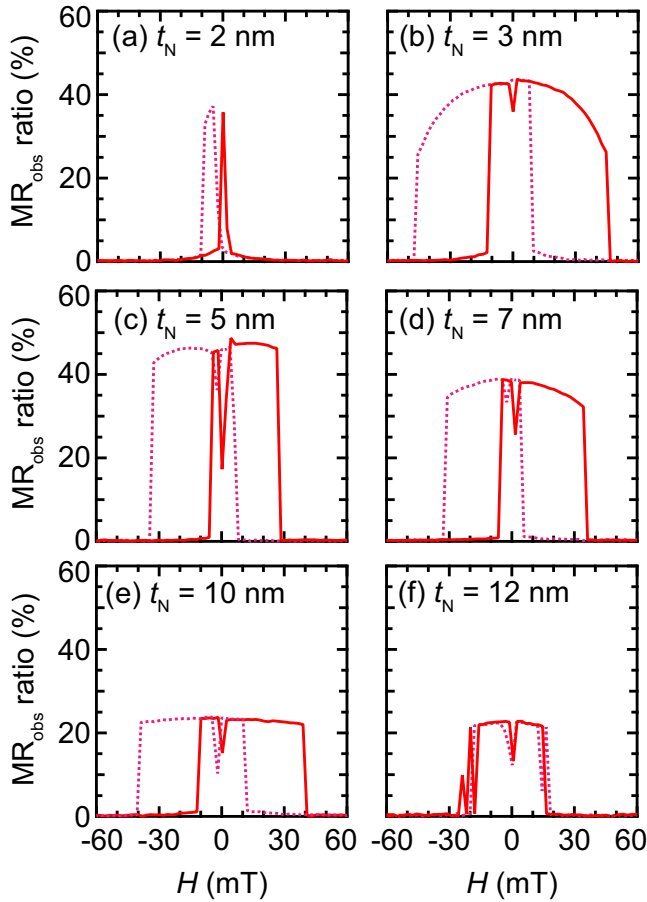


FIG. 1. Spacer thicknesses t_N dependence of magnetoresistance (MR) curves for $\text{Co}_2\text{Fe}_{0.4}\text{Mn}_{0.6}\text{Si}$ (CFMS) | $L_{12}\text{Ag}_3\text{Mg}$ | CFMS junctions, series A. $t_N =$ (a) 2, (b) 3, (c) 5, (d) 7, (e) 10, and (f) 12 nm. MR ratios are plotted in the observed value, MR_{obs} , which is defined by Eq. (1). The horizontal axis is the applied magnetic field, H .

carried out after the deposition of the upper CFMS layer to promote the chemical ordering of the CFMS layers, and the temperature T_{anneal} was varied from 450 to 650 °C, in 50 °C increments. In the following parts, the samples were classified into two series, A and B, as listed in Table I for investigations of t_N dependence and T_{anneal} dependence, respectively.

The layered films were patterned into a submicrometer-scale pillar shape using electron-beam lithography and argon

TABLE I. The classification and fabrication conditions for the samples in this study.

	Purpose	t_N (nm)	T_{anneal} (°C)
Series A	t_N dependence	2–12	500 (fixed)
Series B	T_{anneal} dependence	5 (fixed)	450–650

ion dry etching. Designed pillar sizes ranged from $50 \times 100 \text{ nm}^2$ to $400 \times 800 \text{ nm}^2$ with a rectangular shape. Actual pillar sizes were estimated using the same method as that in our previous studies [31,33]: cross-sectional views of pillars taken by high-angle annular dark-field scanning transmission electron microscopy (HAADF-STEM) and top views by scanning electron microscopy. Using the actual device sizes, RA and a parasitic resistance R_{para} were estimated from a slope and an intercept, respectively, of the plots of the junction resistance as a function of the inverse device area at parallel magnetization configuration, respectively. In this paper, two definitions are used for the MR ratio: the observed MR ratio (MR_{obs}) and the intrinsic MR ratio (MR_{int}), which are defined as follows:

$$\text{MR}_{\text{obs}} = \frac{R_{\text{AP}} - R_{\text{P}}}{R_{\text{P}}} \times 100(\%), \quad (1)$$

$$\text{MR}_{\text{int}} = \frac{R_{\text{AP}} - R_{\text{P}}}{R_{\text{P}} - R_{\text{para}}} \times 100(\%), \quad (2)$$

where $R_{\text{P(AP)}}$ represents the junction resistance at a parallel (antiparallel) magnetization configuration. ΔRA is also defined as follows:

$$\Delta RA = (R_{\text{AP}} - R_{\text{P}})A = RA \times \text{MR}_{\text{int}}, \quad (3)$$

where A is the junction size.

The MR effects were measured by the four-terminal method at room temperature with an applied bias voltage of approximately 1 mV at the parallel state. The crystal structure of the layered films was characterized by HAADF-STEM and x-ray diffractometry (XRD).

III. RESULTS AND DISCUSSION

A. Spacer-thickness dependence

MR curves are shown in Fig. 1 for series A. The measurement sequence was as follows: (1) A constant applied current was set so that the bias voltage was about 1 mV at a parallel

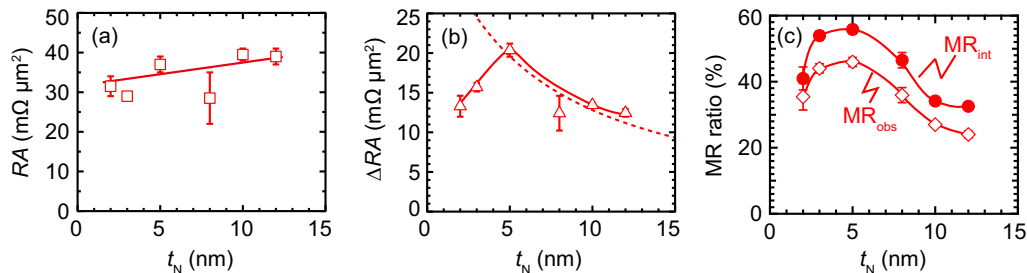


FIG. 2. t_N dependence of (a) RA , (b) ΔRA , and (c) the observed MR ratio MR_{obs} and the intrinsic MR ratio MR_{int} of the junctions. MR_{int} is defined by Eq. (2). The solid lines are a guide to the eyes and a broken line is a fitting line using a model by Valet and Fert [40] for the decay in (b).

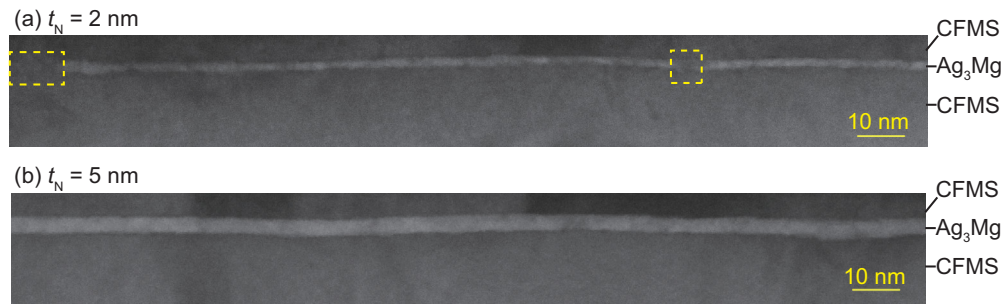


FIG. 3. Cross-sectional high-angle annular dark-field scanning transmission electron microscopy (HAADF-STEM) images of the junctions. $t_N =$ (a) 2 and (b) 5 nm. The 2-nm-thick Ag_3Mg layer is discontinuous in some regions surrounded by dashed squares.

magnetization configuration. (2) The magnetic field was set at -100 mT and the field was swept to $+100$ mT, for which the junction resistance values are plotted as solid lines in Fig. 1. (3) After getting $+100$ mT, the magnetic field was swept to -100 mT, for which the resistance values are plotted as dotted lines in Fig. 1. CPP-GMR is clearly observed for all samples regardless of t_N . MR_{obs} exhibits a maximum value around zero field in most of the curves, which suggests that the upper and the lower CFMS layers are coupled with antiparallel direction to each other because of dipole coupling. Some dips appear around $H \sim 0$. A possible origin of the dips is a multidomain state in the CFMS layers. Here, the size of a pillar is approximately $70 \times 130 \text{ nm}^2$ of a rectangular shape for the MR curves, while the aspect ratio is less than two, which may possibly cause the single-domain-like state to be unstable, especially at the small magnetic field range where the dipolar coupling becomes small. For $t_N = 2$ nm, most junctions showed a peaky curve as shown in Fig. 1(a), suggesting relatively unstable antiparallel magnetization configurations. The switching fields show random variation for $t_N = 3-12$ nm, which is considered to be due to a tiny variation for the edge shapes of the CPP pillars. The variation for the edge shapes was caused by the limited resolution of the electron-beam patterning for the lithography. As a result, the coercivity depends on each pillar.

Figure 2 shows the t_N dependence of RA , ΔRA , MR_{obs} ratio, and MR_{int} ratio for series A. Although there is small data scattering in the dependence of RA , the value is monotonically increases with t_N . On the other hand, ΔRA , MR_{obs} , and MR_{int} ratios exhibit the maximum values at $t_N = 5$ nm.

Concerning the decrease of ΔRA and the MR ratio for $t_N < 5$ nm, the reason is discussed with the results of the structural analysis by HAADF-STEM in the following. Figures 3(a) and 3(b) are low-magnification HAADF-STEM images of the junctions with $t_N = 2$ and 5 nm, respectively. The layered structure and small roughness at CFMS | Ag_3Mg interfaces are confirmed in both images. In addition, especially for $t_N = 2$ nm, there are some discontinuous areas where the CFMS layers contact each other. Although the roughness is of the order of a few angstrom, which is relatively small, the Néel coupling [34,35] may increase with decreasing t_N , which results in increased ferromagnetic coupling between the CFMS layers. Such a situation possibly makes the antiparallel magnetization configuration unstable and results in the decrease of ΔRA and MR ratio for the thin-spacer-thickness junctions. For the present results, the interlayer exchange coupling through the Ag_3Mg spacer is considered to be negligibly small, which

is expected from the small interlayer exchange coupling for layered structures using a Ag spacer [36,37]. In addition to the change in the coupling, the MR properties may degrade in the case that a pillar contains the small discontinuous region in the spacer because of a loss of the spin-dependent transport through the spacer as well as due to the unstable antiparallel magnetization configuration. For $t_N = 3$ nm, the possible Néel coupling contribution is small because, in the MR curve in Fig. 1(b), there are clear high-resistance states. The reason for the degradation of ΔRA and the MR ratios is considered to be due to the spin-independent current passing through the direct contact of the upper and the lower CFMS layers, which may exist similarly to the case for $t_N = 2$ nm. High-resolution HAADF-STEM images are also shown in Figs. 4(a) and 4(b)

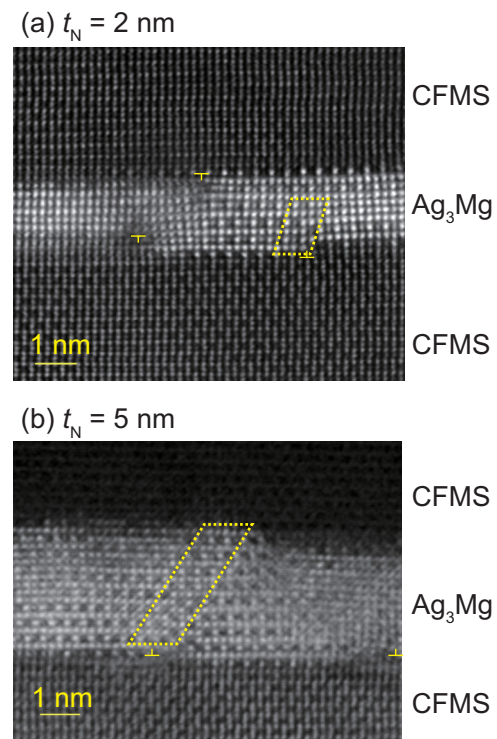


FIG. 4. High-resolution cross-sectional HAADF-STEM images of the junctions with $t_N =$ (a) 2 and (b) 5 nm. Dislocations are marked with \perp or \top at the interfaces. The dotted squares represent the positions of the antiphase boundary. (b) Partly adopted with permission from Ref. [31].

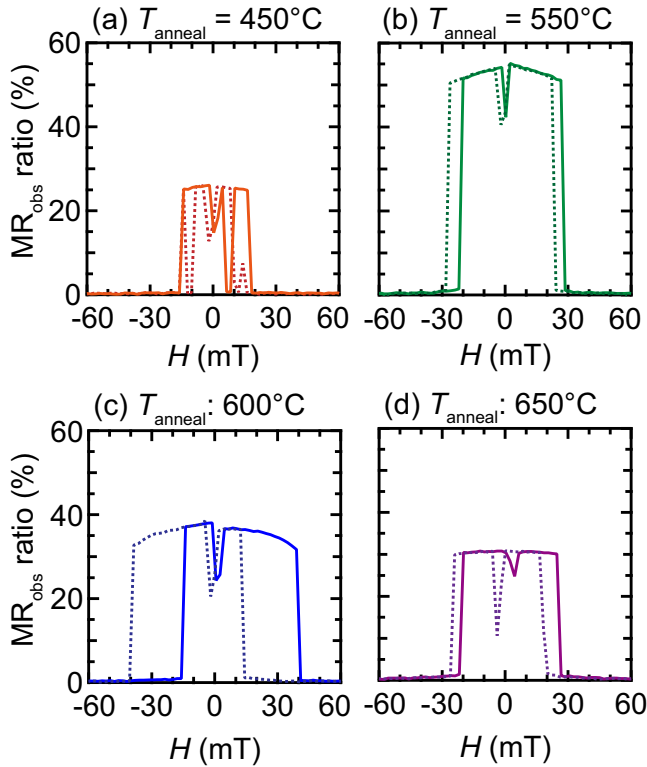


FIG. 5. Annealing temperature T_{anneal} dependence of MR curves for the CFMS $|L1_2 \text{Ag}_3\text{Mg}|$ CFMS junctions, series B. T_{anneal} : (a) 450°C, (b) 550°C, (c) 600°C, and (d) 650°C. $t_N = 5$ nm for all, and the curve for 500°C annealing appeared in Fig. 1(c). MR ratios are plotted in MR_{obs} .

for $t_N = 2$ and 5 nm, respectively. The interfaces between the Ag_3Mg and CFMS layers are well defined for both t_N . Regarding $L1_2$ ordering of the spacer for $t_N = 2$ nm, there are some regions with a low degree of $L1_2$ ordering in the left half of the spacer; however, the difference is quantitatively negligible as compared with that for $t_N = 5$ nm. Thus, the difference of the crystallinity is probably not a reason for the degradation of CPP-GMR in the thin- t_N junctions.

For $t_N \geq 5$ nm, the degradation of CPP-GMR is similarly understood as the previous results in the literature of Co-Fe $|$ Cu $|$ Co-Fe spin valves [38] and the Co-Heusler-based junctions using $B2$ -type NiAl spacer [39] or Cu_2TiAl spacer [19]: The ΔRA and the MR ratios decrease with t_N because

of the finite spin-diffusion length of a spacer material. From the exponential decay of ΔRA , spin-diffusion length l_{sf} of the Ag_3Mg layer is approximately estimated using equations proposed by Valet and Fert [40]. The estimated value of l_{sf} is of the order of 10 to 30 nm, which is one order of magnitude smaller than that reported for pure Mg or Ag in devices with a lateral geometry [41,42]. Although the reason for the short l_{sf} is unclear, a possible factor is a phonon scattering inside the spacer and/or at the interfaces because the resistivity of the spacer is estimated to be about $30 \mu\Omega \text{cm}$ by a linear fitting of the slope of the t_N dependence of RA in Fig. 2(a), which is about six times larger than the bulk value [27]. The large resistivity is considered to originate from phonon scattering induced by misfit dislocations and antiphase boundaries in the spacer, which are marked by \perp or \top and a dotted parallelogram in Fig. 4, respectively. Such scattering may make the mean free path shorter and results in the short l_{sf} [43].

B. Annealing temperature dependence

Figure 5 shows MR curves with various T_{anneal} for series B. The measurement sequence was the same as that for Fig. 1. The shape of all curves suggests that the upper and the bottom CFMS layers are antiferromagnetically coupled to each other by the dipole coupling, similar to the curves in series A. Some dips around $H = 0$ and the variation of the switching fields are considered to originate from the multidomain state and the difference in the shape of pillar edges, respectively, similarly to the results in Fig. 1. Summaries for the T_{anneal} dependence of RA , ΔRA , and MR_{int} ratio are shown in Figs. 6(a)–6(c), respectively. The data points are average values of 10 junctions and the error bars represent the standard deviation of the junctions for the values of ΔRA and MR_{int} ratio.

RA increases monotonically with T_{anneal} . The ΔRA and MR_{int} exhibit a peak at $T_{\text{anneal}} = 550^\circ\text{C}$, at which the maximum values are $25 \pm 2 \text{ m}\Omega \mu\text{m}^2$ and $63 \pm 2\%$, respectively. Concerning the ΔRA value, a record was reported by Jung *et al.* in 2016 in which an average and the highest ΔRA were $25 \text{ m}\Omega \mu\text{m}^2$ and $31 \text{ m}\Omega \mu\text{m}^2$, respectively, using $\text{Co}_2\text{FeGa}_{0.5}\text{Ge}_{0.5}$ electrodes and a Ag spacer tailored with ultrathin NiAl layers at the interfaces [21]. On the basis of the average ΔRA , the present CFMS $|L1_2 \text{Ag}_3\text{Mg}|$ CFMS junctions exhibit comparable CPP-GMR with the reported values in Ref. [21].

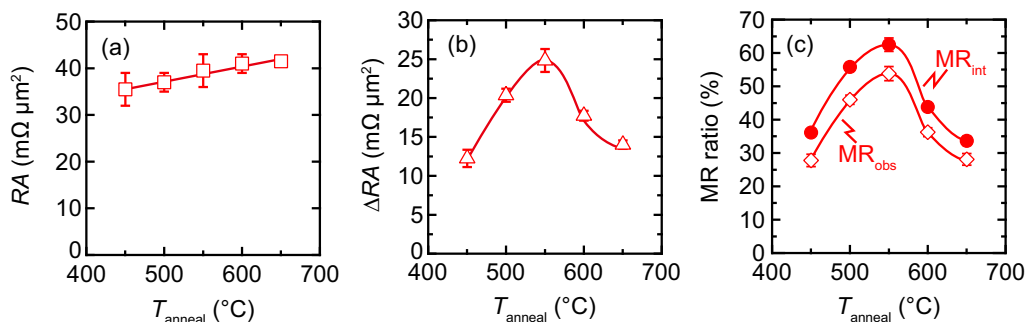


FIG. 6. T_{anneal} dependence of (a) RA , (b) ΔRA , and (c) MR_{int} of the junctions. Solid lines are guides to the eyes.

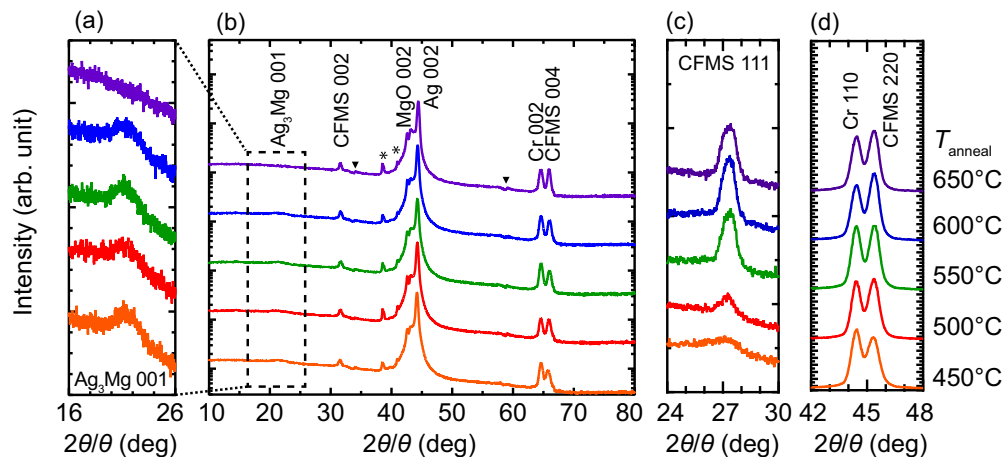


FIG. 7. (a),(b) Out-of-plane and (c),(d) pseudo-in-plane x-ray diffraction (XRD) patterns of the layered films for the junctions. T_{anneal} ranges 450–650 °C from bottom to top. The scans for a superlattice diffraction of Ag_3Mg 001 for the L_2 phase are enlarged in (a). The scans for a CFMS 111 diffraction for the L_2 phase and the fundamental CFMS 220 diffraction are shown in (c) and (d), respectively. Peaks marked with * and \blacktriangledown represent diffractions from the MgO substrate (K_α and K_β) and backgrounds, respectively. Note that the vertical axes are plotted in the linear scale for (a) and (c), and the logarithmic scale in (b) and (d).

Concerning the trends in T_{anneal} dependence, it can be explained by the crystallinity of the layered films: the degrees of chemical ordering for the L_2 phase in the Ag_3Mg spacer and L_2 phase in the CFMS layers, as well as the degree of (001) orientation for the CFMS layers. Figure 7 shows XRD patterns of the layered films for the CPP-GMR junctions. The (001) texture and no unexpected phase are confirmed in the patterns with the out-of-plane geometry for all films, as shown in Fig. 7(b). The 001 superlattice diffraction of the L_2 phase of Ag_3Mg appears for some films with T_{anneal} ranging from 450 to 600 °C, and the peak disappears at 650 °C. In addition, the 111 superlattice diffraction of the L_2 phase of CFMS appears for all samples and the intensity changes depending on T_{anneal} , as shown in Fig. 7(c). The spectra for the 220 fundamental diffraction are also shown in Fig. 7(d).

Summaries of the crystallinity for series B are shown in Figs. 8(a)–8(c) for the long-range order parameters for B_2 (S_{B_2}) and L_2 (S_{L_2}) phases of the CFMS layers, the full width at half maximum (FWHM) of the CFMS 002 diffraction, and the integrated intensities of Ag_3Mg 001 diffraction, respectively. Here, the definitions of S_{B_2} and S_{L_2} are as

follows:

$$S_{B_2} = \sqrt{(I_{002}^{\text{exp}}/I_{004}^{\text{exp}})/(I_{002}^{\text{sim}}/I_{004}^{\text{sim}})}, \quad (4)$$

$$S_{L_2} = \sqrt{(I_{111}^{\text{exp}}/I_{202}^{\text{exp}})/(I_{111}^{\text{sim}}/I_{202}^{\text{sim}})}, \quad (5)$$

where $I_{hkl}^{\text{exp(sim)}}$ is the experimental (simulated) integrated intensity of the hkl diffraction.

First, for $T_{\text{anneal}} = 450$ to 550 °C, where both ΔRA and MR_{int} increase with T_{anneal} , the enhancements of S_{L_2} and the (001) orientation in the CFMS layers are the dominant factors: S_{L_2} increases from 0.6 to 0.9 with increasing T_{anneal} from 450 to 500 °C. Although S_{L_2} maintains almost a constant value in the range of T_{anneal} from 500 to 600 °C, ΔRA and MR_{int} keep increasing up to the T_{anneal} of 550 °C. The difference between the junctions with T_{anneal} of 500 and 550 °C is FWHM of the CFMS 002 diffraction, which decreases drastically with increasing T_{anneal} from 450 to 550 °C. Note that $I_{\text{Ag}_3\text{Mg}001}$ shows a small increase with T_{anneal} from 450 to 500 °C, which also contributes to the enhancement of the CPP-GMR. Second, for $T_{\text{anneal}} = 550$ to 600 °C, degradation of S_{B_2} , S_{L_2} , and

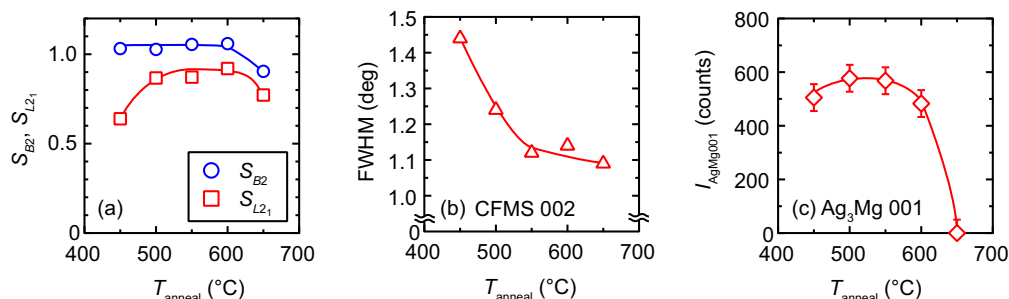


FIG. 8. T_{anneal} dependence of (a) the long-range order parameters for B_2 (S_{B_2}) and L_2 (S_{L_2}) phases of the CFMS layers, (b) full width at half maximum (FWHM) of the CFMS 002 diffraction, and (c) the integrated intensity of the Ag_3Mg 001 diffraction, $I_{\text{Ag}_3\text{Mg}001}$. S_{B_2} and S_{L_2} are defined by Eqs. (4) and (5), respectively.

I_{AgMg001} cause the decrease of the the CPP-GMR: S_{B2} and S_{L2_1} decreases at T_{anneal} of 650°C , and I_{AgMg001} starts to decrease from T_{anneal} of 600°C . These results suggest the degradation of chemical ordering as well as the interface properties, which results in the decrease of ΔRA and MR_{int} ratio after the high-temperature annealing.

IV. SUMMARY

The spacer thickness and the annealing temperature dependence of CPP-GMR effects were investigated in CFMS $|L1_2\text{Ag}_3\text{Mg}|$ CFMS junctions. In the t_N dependence, both ΔRA and MR_{int} ratio exhibited the maximum values at $t_N = 5$ nm. For $t_N < 5$ nm, the decrease of the CPP-GMR is considered to originate from an unstable antiparallel magnetization configuration, which is possibly caused by the enhancement of Néel coupling. For $t_N > 5$ nm, the CPP-GMR decreased due to the finite spin-diffusion length of the Ag_3Mg spacer. An approximate value of the spin-diffusion length of the spacer was also estimated using the decay of ΔRA

in the thick-spacer region based on the Valet-Fert formula [40], which was found to be of the order of 10–30 nm. The estimated spin-diffusion length is relatively short compared with that of pure Ag or Mg in the literature [41,42]. In the T_{anneal} dependence, both ΔRA and MR_{int} ratio exhibited the maximum values at $T_{\text{anneal}} = 550^\circ\text{C}$. The T_{anneal} dependence correlates with the degrees of order in CFMS layers and the Ag_3Mg layer, as well as the (001) orientation of the CFMS layers. The maximum ΔRA and MR_{int} ratio were $25 \text{ m}\Omega \mu\text{m}^2$ and 63%, respectively, at room temperature.

ACKNOWLEDGMENTS

This work was partially supported by Grant-in-Aid for Scientific Research(S), Grant No. 25220910, from the Japan Society for the Promotion of Science, and Advanced Storage Research Consortium (ASRC). This work was a part of a cooperative program (Grant No. 16G0407) of the CRDAM-IMR, Tohoku University. The Foundation for Promotion of Material Science and Technology of Japan are acknowledged for HAADF-STEM observations.

-
- [1] 2016 ASTC Technology Roadmap, The International Disk Drive Equipment and Materials Association, <http://fidema.org/> (unpublished).
- [2] A. Hirohata, H. Sukegawa, H. Yanagihara, I. Žutić, T. Seki, S. Mizukami, and R. Swaminathan, *IEEE Trans. Magn.* **51**, 0800511 (2015).
- [3] M. Takagishi, K. Koi, M. Yoshikawa, T. Funayama, H. Iwasaki, and M. Sahashi, *IEEE Trans. Magn.* **38**, 2277 (2002).
- [4] M. Takagishi, K. Yamada, H. Iwasaki, H. Fuke, and S. Hashimoto, *IEEE Trans. Magn.* **46**, 2086 (2010).
- [5] K. Yakushiji, K. Saito, S. Mitani, K. Takanashi, Y. K. Takahashi, and K. Hono, *Appl. Phys. Lett.* **88**, 222504 (2006).
- [6] Y. Sakuraba, T. Iwase, K. Saito, S. Mitani, and K. Takanashi, *Appl. Phys. Lett.* **94**, 012511 (2009).
- [7] T. Furubayashi, K. Kodama, H. Sukegawa, Y. K. Takahashi, K. Inomata, and K. Hono, *Appl. Phys. Lett.* **93**, 122507 (2008).
- [8] T. Iwase, Y. Sakuraba, S. Bosu, K. Saito, S. Mitani, and K. Takanshi, *Appl. Phys. Express* **2**, 063003 (2009).
- [9] N. Hase, B. S. D. Ch. S. Varaprasad, T. M. Nakatani, H. Sukegawa, S. Kasai, Y. K. Takahashi, T. Furubayashi, and K. Hono, *J. Appl. Phys.* **108**, 093916 (2010).
- [10] M. J. Carey, S. Maat, S. Chandrashekariaih, J. A. Katine, W. Chen, B. York, and J. R. Childress, *J. Appl. Phys.* **109**, 093912 (2011).
- [11] T. M. Nakatani, S. Mitani, T. Furubayashi, and K. Hono, *Appl. Phys. Lett.* **99**, 182505 (2011).
- [12] J. Sato, M. Oogane, H. Naganuma, and Y. Ando, *Appl. Phys. Express* **4**, 113005 (2011).
- [13] Y. Sakuraba, M. Ueda, Y. Miura, K. Sato, S. Bosu, K. Saito, M. Shirai, T. J. Konno, and K. Takanashi, *Appl. Phys. Lett.* **101**, 252408 (2012).
- [14] S. Li, Y. K. Takahashi, T. Furubayashi, and K. Hono, *Appl. Phys. Lett.* **103**, 042405 (2013).
- [15] Y. Sakuarba, M. Ueda, S. Bosu, K. Saito, and K. Takanashi, *J. Magn. Soc. Jpn.* **38**, 45 (2014).
- [16] H. Yako, Y. Sakuraba, K. Amemiya, M. Sakamaki, T. Kubota, T. Sasaki, Y. Miura, K. Hono, and K. Takanashi (unpublished).
- [17] Y. Sakuraba, K. Izumi, T. Iwase, S. Bosu, K. Saito, K. Takanashi, Y. Miura, K. Futatsukawa, K. Abe, and M. Shirai, *Phys. Rev. B* **82**, 094444 (2010).
- [18] K. Nikolaev, P. Kolbo, T. Pokhil, X. Peng, Y. Chen, T. Ambrose, and L. Mrysaov, *Appl. Phys. Lett.* **94**, 222501 (2009).
- [19] S. Li, Y. K. Takahashi, Y. Sakuraba, J. Chen, T. Furubayashi, O. Mrysov, S. Faleev, and K. Hono, *J. Appl. Phys.* **119**, 093911 (2016).
- [20] N. Hase, T. M. Nakatani, S. Kasai, Y. K. Takahashi, T. Furubayashi, and K. Hono, *J. Magn. Mater.* **324**, 440 (2012).
- [21] J. W. Jung, Y. Sakuraba, T. T. Sasaki, Y. Miura, and K. Hono, *Appl. Phys. Lett.* **108**, 102408 (2016).
- [22] T. Furubayashi, Y. K. Takahashi, T. T. Sasaki, and K. Hono, *J. Appl. Phys.* **118**, 163901 (2015).
- [23] T. Nakatani, G. Mihajlovic, J. C. Read, Y. S. Choi, and J. R. Childress, *Appl. Phys. Express* **8**, 093003 (2015).
- [24] S. Kasai, Y. K. Takahashi, P.-H. Cheng, Ikhtiar, T. Ohkubo, K. Kondou, Y. Otani, S. Mitani, and K. Hono, *Appl. Phys. Lett.* **109**, 032409 (2016).
- [25] K. Mukaiyama, S. Kasai, Y. K. Takanashi, K. Kondou, Y. Otani, S. Mitani, and K. Hono, *Appl. Phys. Express* **10**, 013008 (2017).
- [26] K. Masuda and Y. Miura, *Jpn. J. Appl. Phys.* **56**, 020306 (2017).
- [27] K. Fujiwara, M. Hirabayashi, D. Watanabe, and S. Ogawa, *J. Phys. Soc. Jpn.* **13**, 167 (1958).
- [28] H. Okamoto, in *Ag-Mg Phase Diagram*, ASM Alloy Phase Diagrams Database, edited by H. Okamoto and K. Cenual (ASM International, Materials Park, OH, 2016).
- [29] H. Narisawa, T. Kubota, and K. Takanashi, *Appl. Phys. Express* **8**, 063008 (2015).
- [30] H. Narisawa, T. Kubota, and K. Takanashi, *Appl. Phys. Express* **8**, 119201 (2015).

- [31] T. Kubota, Y. Ina, M. Tsujikawa, S. Morikawa, H. Narisawa, Z. Wen, M. Shirai, and K. Takanashi, *J. Phys. D: Appl. Phys.* **50**, 014004 (2017).
- [32] Z. Wen, T. Kubota, Y. Ina, and K. Takanashi, *Appl. Phys. Lett.* **110**, 102401 (2017).
- [33] H. Narisawa, T. Kubota, and K. Takanashi, *Appl. Phys. Express* **8**, 119102 (2015).
- [34] L. Néel, *C. R. Acad. Sci. (Paris)* **255**, 1676 (1962).
- [35] J. C. S. Kools, *IEEE Trans. Magn.* **32**, 3165 (1996).
- [36] S. S. P. Parkin, *Phys. Rev. Lett.* **67**, 3598 (1991).
- [37] S. Bosu, Ph.D. dissertation, Tohoku University, 2009.
- [38] N. Tezuka, S. Abe, Y. Jiang, and K. Inomata, *J. Magn. Magn. Mater.* **290-291**, 1150 (2005).
- [39] T. Nakatani, Ph.D. dissertation, University of Tsukuba, 2011.
- [40] T. Valet and A. Fert, *Phys. Rev. B* **48**, 7099 (1993).
- [41] H. Idzuchi, Y. Fukuma, L. Wang, and Y. Otani, *Appl. Phys. Express* **3**, 063002 (2010).
- [42] Y. Fukuma, L. Wang, H. Idzuchi, S. Takahashi, S. Maekawa, and Y. Otani, *Nat. Mater.* **10**, 527 (2011).
- [43] J. M. D. Coey, *Magnetism and Magnetic Materials* (Cambridge University Press, Cambridge, 2010), Chap. 14, pp. 497–501.